![University of Glasgow logo]

http://eprints.gla.ac.uk/216673/

Deposited on 28 May 2020

Optimization of Sintering Process on $Li_{1+x}Al_xTi_{2-x}(PO_4)_3$ Solid Electrolytes for All-Solid-State Lithium-ion Batteries

Pei-Yi Yen,[a] Meng-Lun Lee,[b] Duncan H. Gregory[c],* and Wei-Ren Liu[a],*

[a] Department of Chemical Engineering, Chung Yuan Christian University, 200 Chung Pei Road, Chungli District, Taoyuan City, 32023, Taiwan, R.O.C.

[b] New Bettery Energy Technology Co., Ltd., Chungli District, Taoyuan City, 32023, Taiwan, R.O.C.

[c] WestCHEM, School of Chemistry, University of Glasgow, Glasgow G12 8QQ UK

*E-mail address: WRLiu1203@gmail.com; Duncan.Gregory@glasgow,ac,uk

Tel:+886 3-265-4140; fax: +886 3-265-4199

Abstract

In this study, a NASICON-structured $Li_{1.3}Al_{0.3}Ti_{1.7}(PO_4)_3$ (LATP) powder is prepared by hydrothermal methods followed by calcination, cold pressing and post-sintering processes. The white, solid product is characterized thoroughly using powder X-ray diffraction (XRD) and field emission scanning electron microscopy (FE-SEM) equipped with Energy Dispersive X-ray Spectroscopy (EDS). The conductivity of the material is measured by a impedance spectroscopy as a function of temperature. Initially, hydrothermal synthesis yields a material isostructural with the orthorhombic oxyphosphate, $LiTiOPO_4$. EDS analysis shows that the distribution of aluminum throughout this material is uniform. A systematic study is then performed to investigate how altering the sintering parameters (such as powder pre-sintering temperature and pellet sintering

1

temperature) affect the formation of LATP. The structure is determined by Rietveld refinement against XRD data and the effects of sintering temperature on porosity, microstructure and electrical conductivity were resolved. The experimental results show that the optimum pre-sintering and sintering temperatures of LATP powders and pellets respectively are 900 °C and 1100 °C. These conditions produce materials with the highest density (99.07% of theoretical), superior conductivity (grain-, grain boundary- and total lithium-ion conductivities of 6.57×10^{-4}, 4.59×10^{-4} and 2.70×10^{-4} S cm^{-1}, respectively) and with an activation energy for Li motion of 0.17 eV.

Keywords: NASICON; $Li_{1.3}Al_{0.3}Ti_{1.7}(PO_4)_3$; solid electrolyte; ionic conductivity; sintering process; lithium-ion batteries

1. Introduction

Since the commercialization of lithium ion batteries (LIBs), LIBs have been widely used as power sources for portable electronic devices due to their high energy density, light weight and long cycle life. However, LIBs containing organic liquid electrolytes have problems with leakage and flammability, which particularly limits large-scale applications. Use of solid-state electrolytes (SSEs) in all-solid-state-batteries (ASSBs) is expected to counteract many of the present safety problems of lithium-ion batteries due to the minimization of unwanted reactivity at the electrode interfaces.

Many kinds of inorganic solid state electrolytes, such as garnet-type $Li_7La_3Zr_2O_{12}$[1-5], perovskite-type $Li_{3x}La_{2/3-x}TiO_3$[6-10], and Na-superionic conductor (NASICON)-type systems[11-15] are being actively investigated. Among them, the NASICON-type material, lithium titanium phosphate, $LiTi_2(PO_4)_3$ (LTP) is considered one of the most promising solid-state electrolytes given its inherent safety, low cost, high thermal and air stability at room temperature. In addition, LTP has proved to be an adaptable material, with use as an effective electrolyte not

only in all-solid-state lithium-ion batteries (ASSLBs)[16-18], but also in lithium-air [19, 20] and lithium-sulfide systems[21].

NASICON-type $LiTi_2(PO_4)_3$ forms with a rhombohedral structure composed of octahedral TiO_6 which corner-share with tetrahedral PO_4. Two types of Li cation vacancies exist in the structure; M1 vacancies, which are formed between tetrahedral PO_4 and M2 vacancies, which are formed between adjoining octahedral TiO_6. In a 3-D NASICON network[22, 23], Li^+ ions diffuse along the pathways which interconnect the M1–M2 vacancies.

The disadvantage with $LiTi_2(PO_4)_3$, however, is lower ionic conductivity at room temperature[24]. In LTP, the contribution of the grain boundary resistance to the total resistance is much larger than that contributed by the bulk. In other words, the grain boundary resistance is the major factor that governs the total conductivity of $LiTi_2(PO_4)_3$. Therefore, controlling the density of an LTP electrolyte becomes a key factor towards optimizing the total conductivity. In order to increase the density, many researchers have begun to study the effects of adding fluxes or employing new sintering techniques, for example, some of which are discussed briefly below[25].

It has been found that Ti^{4+} can be replaced by various trivalent elements (such as Al^{3+}, Fe^{3+}, Y^{3+}, Cr^{3+}, Ga^{3+} and Sc^{3+}) while retaining the rhombohedral NASICON-type structure [17, 26-28]. Among these aliovalent substituents, Al^{3+} appears to modify the NASICON cell volume towards its optimum size for facile Li^+ transport and significantly improves the conductivity in so-formed $Li_{1+x}Al_xTi_{2-x}(PO_4)_3$ (LATP). Conversely, some studies have emphasized that a major role of the aluminum additive is to form the Al-rich second phase $AlPO_4$, which improves the total ion conductivity by enhancing densification effectively forming a composite. However, the concentration of added Al is crucial since at high levels it acts so as to prevent Li-ion conduction across the $LiTi_2(PO_4)_3$ grain boundaries. Thus, maintaining an overall control of the LTP

microstructure would appear to be vital in efforts to maximize overall conductivity; a balance needs to be struck between achieving high density and ensuring secondary phases do not impede ionic transport at the grain boundaries[29].

An alternative approach to this microstructure problem is to employ low melting point fluxes[24, 30-32] to densify LTP and associated substituted solid electrolytes.. In early research of this type, Aono *et al*.[24] used inorganic binders, such as Li_2O and $Li_4P_2O_7$, as fluxes to increase the relative density of the sintered pellets and the Li^+ concentration at the grain boundaries; the ionic conductivity was increased to 3.5×10^{-4} S cm^{-1} as a result. Aono *et al*.[30] went on to use other fluxes, including Li_3PO_4 and Li_3BO_3, to reduce the activation energy of Li^+ grain boundary diffusion and to increase the contact area between the crystal grains. The LTP-0.2 Li_3BO_3 sample showed an ion conductivity of 3.0×10^{-4} S cm^{-1} at room temperature. In more recent research, Bai *et al*.[31], found that $LiBO_2$ could act as a very effective sintering aid, which densifies LATP and improves the Li-ion conductivity as a consequence. The LATP-$LiBO_2$ material forms a uniform microstructure with a relative density of up to 97.1% of the theoretical value and a total ionic conductivity of 3.5×10^{-4} S cm^{-1}, the activation energy for Li^+ motion was reduced to 0.39 eV.

The focus of recent research has switched to employing different sintering techniques to prepare LTP and LATP without sintering aids. These include melt quenching[33, 34], sol-gel[11, 13, 35], mechanical milling[36, 37], co-precipitation[38, 39] and spark plasma sintering (SPS)[40-43] techniques. Kobayashi *et al*.[43] found out that the Li-ion conductivity in LTP at room temperature can be improved from 10^{-8} to 10^{-6} S cm^{-1} *via* the SPS process. In an alternative approach, Xu *et al* prepared high density LATP ($x = 0.4$) with ~ 100% of theoretical density by hydrothermal methods [41]. The resulting material possessed an exceptionally high ionic

conductivity of 1.12×10^{-3} S cm^{-1} at room temperature and a corresponding low activation energy of 0.25 eV for Li-ion motion.

2. Experimental

2.1. LATP synthesis and pellet preparation

Ti(OCH(CH$_3$)$_2$)$_4$ (Acros, purity, 98%), Al(NO$_3$)$_3$·9H$_2$O (Shimakyu's pure chemical Co, Ltd., 98%), H$_3$PO$_4$ (Echo chemical Co, Ltd., 86%) and LiOH·H$_2$O (Acros, 98%) were used without further purification and simply mixed with a molar ratio of Li:Al:Ti:P = 1.3:0.3:1.7:3. 60 ml of the resulting mixture was transferred into a 100 ml stainless steel autoclave. The autoclave was sealed, and heated to 180 ℃ in a furnace (Thermo®, BF51314C) for 24 h before cooling to room temperature. The resulting product was filtered, washed with deionized water and ethanol (Echo chemical Co, Ltd., 95%). The LATP precursor cake was dried for 12 h at 80 ℃ and the solid (named "**LATP-pre**") characterized before further treatment. The dry powder was split into 5 samples and heated in air for 3 h at 500 ℃ (named "**LATP-500**"), 600 ℃ ("**LATP-600**"), 700 ℃ ("**LATP-700**"), 800 ℃ ("**LATP-800**") and 900 ℃("**LATP-900**"), respectively. After cooling, each of the LATP powders was cold pressed at 13000 psi to a pellet of a diameter and thickness of *ca*.10 mm and 1.5 mm, respectively. The pellets were sintered at 900 ℃, 1000 ℃, 1100 ℃ and 1200 ℃ for 3 h in air, respectively. Each of these pellets are denoted herein in terms of their initial heating and final sintering temperatures (e.g. "**LATP-500-900**" etc.)

2.2. Characterization

The two faces of each pellet were polished and painted with silver paste as blocking electrodes. The AC impedance was measured using a Solartron (SI1287+1255B) Impedance Analyzer in the frequency range from 1 MHz - 0.01 Hz, with AC amplitude of 30 mV. The measurements were performed at temperatures from 25 ℃ - 125 ℃. The dried precursor powders and the product

pellets were characterized by powder X-ray diffraction (XRD; Bruker D8 Advance Eco) with Cu Kα radiation ($\lambda = 1.5418$ Å). Rietveld structure refinement against XRD data was performed using the GSAS software[44]. The morphology and structure of the LATP sample was analyzed using Ultra-High Resolution Field Emission Scanning Electron Microscope (FE-SEM; JEOL/JSM-7600F) equipped with energy dispersive X-ray spectroscopy (EDS). Thermogravimetric Analyzer (TGA; DuPont, TA Q50) was performed on the LATP-pre power at a heating rate of 10 ℃ min^{-1} in a temperature range of 30–800 ℃ under air atmosphere.

2.3. NCM-LATP/AG pouch cell construction

Electrodes for the pouch cell were provided by Gold Carbon Corp, Ltd. The anode consisted of artificial graphite (AG) (93.8%) active material and polyvinylidene difluoride (PVdF) (Sigma-Aldrich, purity 99%) binder on Cu foil (UBIQ Technology, purity 99%) current collector. The cathode consisted of $LiNi_{0.5}Co_{0.2}Mn_{0.3}O_2$ (NCM-523, NCM) (82%) (Provided from Gold Carbon Company) active material and PVdF binder on Al foil (UBIQ Technology, purity 99%) current collector. A slurry containing LATP and PVdF binder (96:4 wt.%) in NMP (N-methyl pyrrolidinone; UBIQ technology Co. Ltd., 99%) was used to prepare the LATP electrolyte. The LATP slurry was coated on the NCM electrode and dried at 80 ℃, then marked as "NCM-LATP". The NCM-LATP (193.3 mAh, density: 0.0175 g/mm^2) and AG (254 mAh, density: 0.0072 g/mm^2) electrodes were punched and dried at 120 ℃ for 8 h in vacuum to remove the residual water. The electrode sizes of anode and cathode are 25 mm x 25 mm. After pouch cell assembly (A/C ratio is 1.31), the cell was run over 2 cycles at a very slow rate (0.5C). The voltage range of 2.8-4.3 V under 0.5C was used for cycling stability tests. Manufacture and testing of pouch cells were in a closed room with 25℃ in a drying room with air-conditioning.

3. Results and discussion

Fig. 1(a) shows the experimental X-ray diffraction pattern of the **LATP-Pre** powder prepared by the hydrothermal method after drying. As shown in the figure, the peaks in the diffraction pattern could be assigned to that from the orthorhombic structure of $LiTiOPO_4$ (Lithium titanium oxyphosphate, ICSD#39534).

Fig. 1(b) displays the thermogravimetry analysis (TGA) profile and the profile from the differential of the thermogravimetry (DTG) signal for **LATP-Pre**. A weight loss of 7.76 wt.% was measured from the TGA curve across the temperature range of 30 – 800 °C. Since the precursor powder of hydrothermal synthesis was a crystal phase of $LiTiOPO_4$ with good crystallinity, the main reaction of the precursor powder in the heating process is the transformation of $LiTiOPO_4$ crystal phase into $Li_{1.3}Al_{0.3}Ti_{1.7}(PO_4)_3$ crystal phase, so the weight loss was very small. From the DTG curve we observed six peaks of mass loss. The first broad peak occurred at 50 to 360°C and was a slow endothermic process due to the decomposition of the adsorbed water in the sample. The second peak on the DSC curve was about 402°C. It was caused by the decomposition of organic matter in the precursor powder. As the temperature gradually increases, there was one at 463, 550, 640, and 685°C. The endothermic peak was a process in which the orthorhombic phase of the orthorhombic $LiTiOPO_4$ was gradually converted into a trigonal $Li_{1.3}Al_{0.3}Ti_{1.7}(PO_4)_3$ phase.

Fig. 2(a) shows an FE-SEM image of the **LATP-pre** powder obtained following its recovery after hydrothermal synthesis. It can be clearly observed from the micrograph that **LATP-pre** takes the form of irregular, approximately rectangular plates in the nanometer regime, where the edge of each plate is approximately 80-130 nm in size. In turn, each plate is composed of smaller nanoparticles which can be just discerned from the image at the magnification of 9000X. Figs. 2(b-e) present the EDS mapping for each of the elements except Li from the image shown in Fig.

2(a). The distribution of each element across agglomerations of plates was uniform and homogeneous.

The XRD patterns of the **LATP-pre** precursor after calcination at different temperatures (from 500-900 °C for 3 hours) are shown in Fig. 3(a). The main peaks in the XRD patterns of **LATP-500**, **LATP-600** and **LATP-700** could be indexed as $LiTiOPO_4$ (ICSD#39534). As the temperature increases, the phase composition gradually changes, such that at high sintering temperatures, (**LATP-800** and **LATP-900,)** the main peaks in the diffraction patterns could be indexed as the $Li_{1.3}Al_{0.3}Ti_{1.7}(PO_4)_3$ NASICON-type structure (ICSD#257190) in rhombohedral space group of $R\overline{3}c$.

The effect of temperature on the phase composition of the LATP sample was investigated further by analyzing the diffraction data by Rietveld refinement. Table S1 lists the phase compositions of the various LATP samples after Rietveld refinement analysis. These phase composition data are plotted in Fig. 3(b). As the powder calcination temperature increases, orthorhombic $LiTiOPO_4$ is gradually transformed into the rhombohedral $Li_{1.3}Al_{0.3}Ti_{1.7}(PO_4)_3$ NASICON-type phase and once a powder calcination temperature of 800 °C was reached, the content of the $LiTiOPO_4$ phase dropped from the value of 90.2 wt% observed at the lowest calcination temperature (500 °C) to 14 wt%. On increasing the powder calcination temperature further to 900 °C, there was no further trace of the $LiTiOPO_4$ phase and the content of $Li_{1.3}Al_{0.3}Ti_{1.7}(PO_4)_3$ reaches a maximum (of 81 wt%).

The total impedance was obtained by fitting the respective semicircles from spectra using an equivalent circuit model as shown in the inset of Fig 4. In the fitted circuit, R_b was interpreted as the circuit resistance external to the specimen, which originated from the intercept of the semicircle

with the Z' axis in the high frequency region and was taken as representing the bulk resistance. R_{gb} was defined as the grain boundary resistance.

Each of the calcined powders except LATP-1000 was pelletized and sintered at 900 °C for 3 h. These are hereafter denoted **LATP-500-900**, **LATP-600-900**, **LATP-700-900**, **LATP-800-900** and**LATP-900-900**. The bulk, grain boundary and total conductivities of all samples sintered at 900 °C for 3h are listed in Table 1. As the calcination temperature (i.e. *pre*-sintering treatment temperature) increases, the impedance notably decreases. Consequently, **LATP-900-900** exhibited the highest total ionic conductivity (σ_{total}) and relative density of $5.72*10^{-5}$ S cm^{-1} and 94.10%, respectively, at room temperature.

Fig. 5(a)-(e) displays SEM images of samples of the **LATP-500**, **LATP-600**, **LATP-700**, **LATP-800** and **LATP-900** powders. The grain size was about 110-162 nm, 71-78 nm, 95-160 nm, 230-370 nm, 150-225 nm. Although there is not a clear trend of increasing particle size with calcining temperature, it is evident from the SEM images that at lower calcining temperatures the samples were composed of particles that were more three-dimensional and less anisoptropic in nature. At 500 °C, for example, the irregular cuboid crystallites are stacked rather inefficiently, leaving relatively large interparticle voids and creating a macroporous microstructure. As the calcination temperature is raised, the particles themselves become more two-dimensional, anisotropic and plate-like. Further, the platelets agglomerate such that the interparticle porosity progressively decreases. By 900 °C, the density of the material has visibly increased in the SEM images. Fig. 5(f) shows the EDS spectrum from **LATP-900**. The experimental values measured for **LATP-900** are very close to the theoretical values and consistent with the ratios of starting materials used to make the desired LATP product. Combined, from the results of EDS elemental mapping, area scans and point scans, one can infer from the uniform distribution of elements in

the correct stoichiometric ratio, that the samples consist of agglomerated particles of $Li_{1.3}Al_{0.3}Ti_{1.7}(PO_4)_3$.

After confirming that 900 °C was the preferred calcination temperature for the powders (i.e. that the **LATP-900-900** sample was the best of the sintered samples), further studies were pursued to explore the effect of the sintering temperature (i.e. second heat treatment temperature) on the microstructure and transport properties of the LATP samples. The **LATP-900** powder was pelletized and sintered at 900 °C, 1000 °C, 1100 °C, 1200 °C and 1300°C for 3 h (and will be referred to as: **LATP-900-900**, **LATP-900-1000**, **LATP-900-1100**, **LATP-900-1200** and**LATP-900-1300** respectively). The sample sintered at 1300 °C, however, was discarded as the sintering temperature had evidently exceeded the melting point of the material.

Fig. 6(a) compiles the Nyquist plots from the AC impedance analysis of all the LATP pellets measured at 25 °C and the bulk, grain boundary and total conductivities of all samples are displayed in Table 2. Results demonstrate that as the sintering temperature is increased so the total Li-ion conductivity increases until a maximum of $2.70×10^{-4}$ S cm^{-1} is reached at a sintering temperature of 1100 °C (**LATP-900-1100**) . Similarly, the grain boundary resistance decreases over the same temperature range and **LATP-900-1100** has the maximum grain boundary conductivity($4.59×10^{-4}$ S cm^{-1}) Both the grain boundary conductivity and total conductivity decrease (to $3.32×10^{-4}$ S cm^{-1} and $2.24×10^{-4}$ S cm^{-1}, respectively) in the sample sintered at 1200 °C (**LATP-900-1200**). Tellingly, these results follow a close correlation with the phase composition data obtained from Rietveld refinements against XRD data taken for the high temperature sintered samples (Table 3). **LATP-900-1100** was found to contain more of the desired rhombohedral fast-ion conducting $Li_{1.3}Al_{0.3}Ti_{1.7}(PO_4)_3$ phase than **LATP-900-1200**, which conversely contained more impurities. In fact, the major difference between the two samples in

this respect is the proliferation of AlPO$_4$ at higher temperature. It is reasonable to assume that despite the improved bulk transport of Li$^+$ in the LATP phase, the increased presence of the phosphate at the LATP grain boundaries is sufficient to block the diffusion of lithium ions, reducing not only the grain boundary conductivity but also the magnitude of the total conductivity. Hence any densification benefits apparently imparted by AlPO$_4$ are rendered counter-productive by the increased grain boundary resistance.

Fig. 6(b) shows the temperature dependence of the conductivity for the high temperature sintered pellets LATP-900-900 – LATP-900-1200 from 25 – 125 ℃. From the resulting Arrhenius plot, the data demonstrate that, the conductivity of all the samples increases with temperature as one would expect and that across the measured temperature range the conductivity improves as the sintering temperature increases.

Fig. 7 collates the FE-SEM micrographs for the high temperature sintered samples (excluding **LATP-900-1300**). The microstructure not only does the size of the individual LATP particles tend to increase with elevated sintering temperature, but also as these particles fuse together, so the density once again increases and the macropores that remain following calcination diminish in number still further.

Fig. 8(a) shows several discharging curves of the NMC-MCMB solid pouch cell between 2.8-4.25V. All the testing procedures were charged with the constant current (CC) protocol at a rate of 0.5C and discharged at different rates, i.e.: 0.5C, 1C, 1.5C, 2C and 2.5C. The capacity values under various C-rates is summarized in Fig. 8(b). The discharge capacity of the cell was 26.5 mAh, 24.9 mAh, and 22.9 mAh at 0.5-, 1- and 1.5-C-rates, respectively. The capacity retention ratio of 1.5C-discharging to 0.5C-discharging is 86%, indicating a stable ionic conductivity under small to medium c-rates. However, the capacity decreased rapidly with the C-rate over 1.5C and was 43%

capacity remain (comparing to 0.5C) at the rate of 2.5C. Obvious capacity decreasing with an increasing discharge C-rate may be explained in terms of the electrochemical polarization due to the increased IR drop. Inset in Fig. 8(b) display cross-sectional SEM image of electrode on cathode side. As shown in this picture, the thickness of LATP layer on the top of NCM was ~100 μm. NCM cathode layer is in between LATP layer and Al foil with a thickness of ~70 μm. Fig. 8(c) shows the plot of charging-discharging capacity as a function of the cycle number for the NMC-MCMB solid pouch cell during a long-term cycling test between 2.8-4.25V. The inset in Fig. 8(c) displays a scheme of the pouch cell in the size of 40mm*50mm to light LED lamp. Identically, the capacity decay of 1st to 100th cycle was only 7%, but the capacity decreasing of 100th to 200th cycle and 200th to 300th cycle was 10% and 13%, respectively. The final capacity at 360th cycle was 16.7mAh, which was 63.2% of the first cycle. The 0.5C discharging curves show similar voltage plateau from 1st to 100th cycle but obvious decay of working voltage from 100th to 300th cycle as demonstrated in Fig. 8(d). Figure 9 displays the cross-sectional SEM image of electrode after 350 cycles. From the observation of SEM image of electrode after cycling tests, the structure of NCM and LATP were integrated and the interface between NCM and LATP was still very clear, which was similar to that of fresh electrode shown in the inset in Fig. 8(b). The result further confirmed the outstanding cycle performance of as-assembled NCM-LATP/MCMB pouch cell.

4. Conclusions

In summary, through the discussion of two-stage sintering. The good contact between the grains and the lower amorphous content of the second phase between the grain boundaries are the key in obtaining high lithium-ion conductivity. The activation energy of LATP-900-1100°C is 0.17 eV, and the relative density is 99.07%. Its grain conductivity, grain boundary conductivity and total

lithium-ion conductivity are $6.57*10^{-4}$, $4.59*10^{-4}$, $2.70*10^{-4}$ S cm^{-1}, respectively. Moreover, we developed a coating method for assembling NCM-LATP/AG pouch cell. The NCM-LATP/AG pouch cell exhibited a high reversible capacity of 16.7 mAh at 0.5 C after 360 cycles with 63.2% capacity retention. The obtained results indicated that LATP is a potential solid electrolyte material could be applied to lithium ion batteries.

Author information

Corresponding Author:

*E-mail address: wrliu1203@gmail.com (W.R. Liu)

References

[1] A. Kaeriyama, H. Munakata, K. Kajihara, K. Kanamura, Y. Sato, T. Yoshida, Evaluation of Electrochemical Characteristics of $Li_7La_3Zr_2O_{12}$ Solid Electrolyte, ECS Transactions 16(24) (2009) 175-180.

[2] M. Kotobuki, H. Munakata, K. Kanamura, Y. Sato, T. Yoshida, Compatibility of $Li_7La_3Zr_2O_{12}$ solid electrolyte to all-solid-state battery using Li metal anode, Journal of The Electrochemical Society 157(10) (2010) A1076-A1079.

[3] R. Murugan, V. Thangadurai, W. Weppner, Fast lithium ion conduction in garnet‐type $Li_7La_3Zr_2O_{12}$, Angewandte Chemie International Edition 46(41) (2007) 7778-7781.

[4] J.-M. Lee, T. Kim, S.-W. Baek, Y. Aihara, Y. Park, Y.-I. Kim, S.-G. Doo, High lithium ion conductivity of $Li_7La_3Zr_2O_{12}$ synthesized by solid state reaction, Solid State Ionics 258 (2014) 13-17.

[5] L. Dhivya, N. Janani, B. Palanivel, R. Murugan, Li+ transport properties of W substituted $Li_7La_3Zr_2O_{12}$ cubic lithium garnets, AIP Advances 3(8) (2013) 082115.

[6] M. Catti, M. Sommariva, R.M. Ibberson, Tetragonal superstructure and thermal history of $Li_{0.3}La_{0.567}TiO_3$ (LLTO) solid electrolyte by neutron diffraction, Journal of Materials Chemistry 17(13) (2007) 1300-1307.

[7] H. Geng, A. Mei, Y. Lin, C. Nan, Effect of sintering atmosphere on ionic conduction and structure of $Li_{0.5}La_{0.5}TiO_3$ solid electrolytes, Materials Science and Engineering: B 164(2) (2009) 91-95.

[8] W.J. Kwon, H. Kim, K.-N. Jung, W. Cho, S.H. Kim, J.-W. Lee, M.-S. Park, Enhanced Li^+ conduction in perovskite $Li_{3x}La_{2/3-x}\square_{1/3-2x}TiO_3$ solid-electrolytes via microstructural engineering, Journal of Materials Chemistry A 5(13) (2017) 6257-6262.

[9] T. Teranishi, Y. Ishii, H. Hayashi, A. Kishimoto, Lithium ion conductivity of oriented $Li_{0.33}La_{0.56}TiO_3$ solid electrolyte films prepared by a sol–gel process, Solid State Ionics 284 (2016) 1-6.

[10] C. Hua, X. Fang, Z. Wang, L. Chen, Lithium storage in perovskite lithium lanthanum titanate, Electrochemistry Communications 32 (2013) 5-8.

[11] M. Kotobuki, M. Koishi, Preparation of $Li_{1.5}Al_{0.5}Ti_{1.5}(PO_4)_3$ solid electrolyte via a sol–gel route using various Al sources, Ceramics International 39(4) (2013) 4645-4649.

[12] G. Kunshina, O. Gromov, E. Lokshin, V. Kalinnikov, Sol-gel synthesis of $Li_{1.3}Al_{0.3}Ti_{1.7}(PO_4)_3$ solid electrolyte, Russian Journal of Inorganic Chemistry 59(5) (2014) 424-430.

[13] T. Hupfer, E. Bucharsky, K. Schell, M. Hoffmann, Influence of the secondary phase LiTiOPO$_4$ on the properties of Li$_{1+x}$Al$_x$Ti$_{2-x}$(PO$_4$)$_3$ (x= 0; 0.3), Solid State Ionics 302 (2017) 49-53.

[14] C. Davis III, J.C. Nino, Microwave Processing for Improved Ionic Conductivity in Li$_2$O–Al$_2$O$_3$–TiO$_2$–P$_2$O$_5$ Glass‑Ceramics, Journal of the American Ceramic Society 98(8) (2015) 2422-2427.

[15] S. Duluard, A. Paillassa, P. Lenormand, P.L. Taberna, P. Simon, P. Rozier, F. Ansart, Dense on porous solid LATP electrolyte system: Preparation and conductivity measurement, Journal of the American Ceramic Society 100(1) (2017) 141-149.

[16] X. Wei, J. Rechtin, E. Olevsky, The Fabrication of All-Solid-State Lithium-Ion Batteries via Spark Plasma Sintering, Metals 7(9) (2017) 372.

[17] P. Zhang, H. Wang, Q. Si, M. Matsui, Y. Takeda, O. Yamamoto, N. Imanishi, High lithium ion conductivity solid electrolyte of chromium and aluminum co-doped NASICON-type LiTi$_2$(PO$_4$)$_3$, Solid State Ionics 272 (2015) 101-106.

[18] J. Liu, T. Liu, Y. Pu, M. Guan, Z. Tang, F. Ding, Z. Xu, Y. Li, Facile synthesis of NASICON-type Li$_{1.3}$Al$_{0.3}$Ti$_{1.7}$(PO$_4$)$_3$ solid electrolyte and its application for enhanced cyclic performance in lithium ion batteries through the introduction of an artificial Li$_3$PO$_4$ SEI layer, RSC Advances 7(74) (2017) 46545-46552.

[19] S. Hasegawa, N. Imanishi, T. Zhang, J. Xie, A. Hirano, Y. Takeda, O. Yamamoto, Study on lithium/air secondary batteries—Stability of NASICON-type lithium ion conducting glass–ceramics with water, Journal of Power Sources 189(1) (2009) 371-377.

[20] Y. Shimonishi, T. Zhang, N. Imanishi, D. Im, D.J. Lee, A. Hirano, Y. Takeda, O. Yamamoto, N. Sammes, A study on lithium/air secondary batteries—Stability of the NASICON-type lithium ion conducting solid electrolyte in alkaline aqueous solutions, Journal of Power Sources 196(11) (2011) 5128-5132.

[21] S. Wang, Y. Ding, G. Zhou, G. Yu, A. Manthiram, Durability of the $Li_{1+x}Ti_{2-x}Al_x(PO_4)_3$ Solid Electrolyte in Lithium–Sulfur Batteries, ACS Energy Letters 1(6) (2016) 1080-1085.

[22] G. Redhammer, D. Rettenwander, S. Pristat, E. Dashjav, C. Kumar, D. Topa, F. Tietz, A single crystal X-ray and powder neutron diffraction study on NASICON-type $Li_{1+x}Al_xTi_{2-x}(PO_4)_3$ ($0 \leq x \leq 0.5$) crystals: Implications on ionic conductivity, Solid State Sciences 60 (2016) 99-107.

[23] D. Rettenwander, A. Welzl, S. Pristat, F. Tietz, S. Taibl, G. Redhammer, J. Fleig, A microcontact impedance study on NASICON-type $Li_{1+x}Al_xTi_{2-x}(PO_4)_3$ ($0 \leq x \leq 0.5$) single crystals, Journal of Materials Chemistry A 4(4) (2016) 1506-1513.

[24] H. Aono, E. Sugimoto, Y. Sadaoka, N. Imanaka, G.y. Adachi, Ionic conductivity of solid electrolytes based on lithium titanium phosphate, Journal of the Electrochemical Society 137(4) (1990) 1023-1027.

[25] H. Aono, E. Sugimoto, Y. Sadaoka, N. Imanaka, G.-y. Adachi, Electrical property and sinterability of $LiTi_2(PO_4)_3$ mixed with lithium salt (Li_3PO_4 or Li_3BO_3), Solid State Ionics 47(3-4) (1991) 257-264.

[26] D.H. Kothari, D.K. Kanchan, P. Sharma, Electrical properties of Li-based NASICON compounds doped with yttrium oxide, Ionics 20(10) (2014) 1385-1390.

[27] D.H. Kothari, D. Kanchan, Effect of doping of trivalent cations Ga^{3+}, Sc^{3+}, Y^{3+} in $Li_{1.3}Al_{0.3}Ti_{1.7}(PO_4)_3$ (LATP) system on Li^+ ion conductivity, Physica B: Condensed Matter 501 (2016) 90-94.

[28] P. Zhang, M. Matsui, Y. Takeda, O. Yamamoto, N. Imanishi, Water-stable lithium ion conducting solid electrolyte of iron and aluminum doped NASICON-type $LiTi_2(PO_4)_3$, Solid State Ionics 263 (2014) 27-32.

[29] S. Yu, A. Mertens, X. Gao, D.C. Gunduz, R. Schierholz, S. Benning, F. Hausen, J. Mertens, H. Kungl, H. Tempel, Influence of microstructure and $AlPO_4$ secondary-phase on the ionic conductivity of $Li_{1.3}Al_{0.3}Ti_{1.7}(PO_4)_3$ solid-state electrolyte, Functional Materials Letters 9(05) (2016) 1650066.

[30] H. Aono, E. Sugimoto, Y. Sadaoka, N. Imanaka, G.-y. Adachi, Electrical property and sinterability of $LiTi_2(PO_4)_3$ mixed with lithium salt (Li_3PO_4 or Li_3BO_3), Solid State Ionics 47(3-4) (1991) 257-264.

[31] H. Bai, J. Hu, X. Li, Y. Duan, F. Shao, T. Kozawa, M. Naito, J. Zhang, Influence of $LiBO2$ addition on the microstructure and lithium-ion conductivity of $Li_{1+x}Al_xTi_{2-x}(PO_4)_3$ (x= 0.3) ceramic electrolyte, Ceramics International 44(6) (2018) 6558-6563.

[32] L. Xiong, Z. Ren, Y. Xu, S. Mao, P. Lei, M. Sun, LiF assisted synthesis of $LiTi_2(PO_4)_3$ solid electrolyte with enhanced ionic conductivity, Solid State Ionics 309 (2017) 22-26.

[33] S. Soman, Y. Iwai, J. Kawamura, A. Kulkarni, Crystalline phase content and ionic conductivity correlation in LATP glass–ceramic, Journal of Solid State Electrochemistry 16(5) (2012) 1761-1766.

[34] J. Fu, Superionic conductivity of glass-ceramics in the system Li_2O-Al_2O_3-TiO_2-P_2O_5, Solid State Ionics 96(3-4) (1997) 195-200.

[35] T. Hupfer, E.C. Bucharsky, K.G. Schell, A. Senyshyn, M. Monchak, M.J. Hoffmann, H. Ehrenberg, Evolution of microstructure and its relation to ionic conductivity in $Li_{1+x}Al_xTi_{2-x}(PO4)_3$, Solid State Ionics 288 (2016) 235-239.

[36] X. Xu, Z. Wen, X. Yang, J. Zhang, Z. Gu, High lithium ion conductivity glass-ceramics in $Li_2O-Al_2O_3-TiO_2-P_2O_5$ from nanoscaled glassy powders by mechanical milling, Solid State Ionics 177(26-32) (2006) 2611-2615.

[37] H. Rusdi, A.R. Azilah, R.H.Y. Subban, N. Mohamed, Characterisation of Lithium Aluminium Titanium Phosphate as Solid Electrolytes Synthesized by Mechanical Milling Method, Advanced Materials Research, Trans Tech Publ, 2012, pp. 190-194.

[38] L. Huang, Z. Wen, M. Wu, X. Wu, Y. Liu, X. Wang, Electrochemical properties of $Li_{1.4}Al_{0.4}Ti_{1.6}(PO_4)_3$ synthesized by a co-precipitation method, Journal of Power Sources 196(16) (2011) 6943-6946.

[39] M. Kotobuki, M. Koishi, Y. Kato, Preparation of $Li_{1.5}Al_{0.5}Ti_{1.5}(PO_4)_3$ solid electrolyte via a co-precipitation method, Ionics 19(12) (2013) 1945-1948.

[40] C.M. Chang, Y.I. Lee, S.H. Hong, H.M. Park, Spark Plasma Sintering of $LiTi_2(PO_4)_3$‐Based Solid Electrolytes, Journal of the American Ceramic Society 88(7) (2005) 1803-1807.

[41] X. Xu, Z. Wen, X. Yang, L. Chen, Dense nanostructured solid electrolyte with high Li-ion conductivity by spark plasma sintering technique, Materials Research Bulletin 43(8-9) (2008) 2334-2341.

[42] R. Kali, A. Mukhopadhyay, Spark plasma sintered/synthesized dense and nanostructured materials for solid-state Li-ion batteries: Overview and perspective, Journal of Power Sources 247 (2014) 920-931.

[43] Y. Kobayashi, T. Takeuchi, M. Tabuchi, K. Ado, H. Kageyama, Densification of $LiTi_2(PO_4)_3$-based solid electrolytes by spark-plasma-sintering, Journal of Power Sources 81 (1999) 853-858.

[44] M. Catti, A. Comotti, S. Di Blas, High-temperature lithium mobility in α-$LiZr_2(PO_4)_3$ NASICON by neutron diffraction, Chemistry of Materials 15(8) (2003) 1628-1632.

Figure Captions

Fig. 1. (a) Experimental XRD pattern of the hydrothermal precursor powder, LATP-pre compared to a calculated XRD pattern of $LiTiO(PO_4)$ taken from crystal data in the Inorganic Crystal Structure Database (ICSD#39534); (b) TGA-DTG profile of the hydrothermal precursor, LATP-pre.

Fig. 2. (a) FE-SEM image of a sample of the hydrothermal precursor, LATP-pre, and (b-e) EDS elemental maps of the same sample; red, light green, cyan and dark blue maps show the presence of P (b), Ti (c), O (d) and Al (e), respectively.

Fig. 3. (a) XRD patterns of LATP powders treated at different calcining temperatures (LATP-500 to LATP-1000) and (b) the quantitative composition of each LATP sample shown as wt% fractions of each crystalline phase, as obtained from Rietveld refinements.

Fig. 5. Nyquist plots from impedance spectroscopy experiments for LATP-500-900, LATP-600-900, LATP-700-900, LATP-800-900 and LATP-900-900 pellets measured at 25 °C. The equivalent circuit that was used to fit the experimental data is show in the inset image.

Fig. 4. FE-SEM images of the products from calcining the LATP-pre precursor powders at (a) 500°C; (b) 600°C; (c) 700°C; (d) 800°C and (e) 900°C; (f) EDS spectrum for the LATP-900 material.

Fig. 6. (a) Nyquist plots and (b) Arrhenius plots from variable temperature impedance spectroscopy experiments on LATP-900-900, LATP-900-1000, LATP-900-1100 and LATP-900-1200 pellets.

Fig. 7. FE-SEM images of LATP-pre powder calcined at 900 °C and then sintered as pellets at temperatures between 900-1200 °C: (a) LATP-900-900, (b) LATP-900-1000, (c) LATP-900-1100 and (d) LATP-900-1200 samples.

Fig. 8. Electrochemical measurements of NCM-LATP/MCMB pouch cells:(a) Charge profile at 0.5C and discharge profiles at 0.5, 1, 1.5, 2 and 2.5C; (b) Capacity versus C-rate. Inset: SEM cross-sectional image of electrode before cycling; (c) Cycling performance at 0.5C for 350 cycles; (d)Discharge curves of the NCM-LATP/MCMB pouch cell in different cycles at 0.5 C.

Fig. 9. SEM cross-sectional images of electrode for NCM-LATP/MCMB pouch cell after 350 cycling testes. Insets: Enlarge the magnitudes of NCM and LATP.
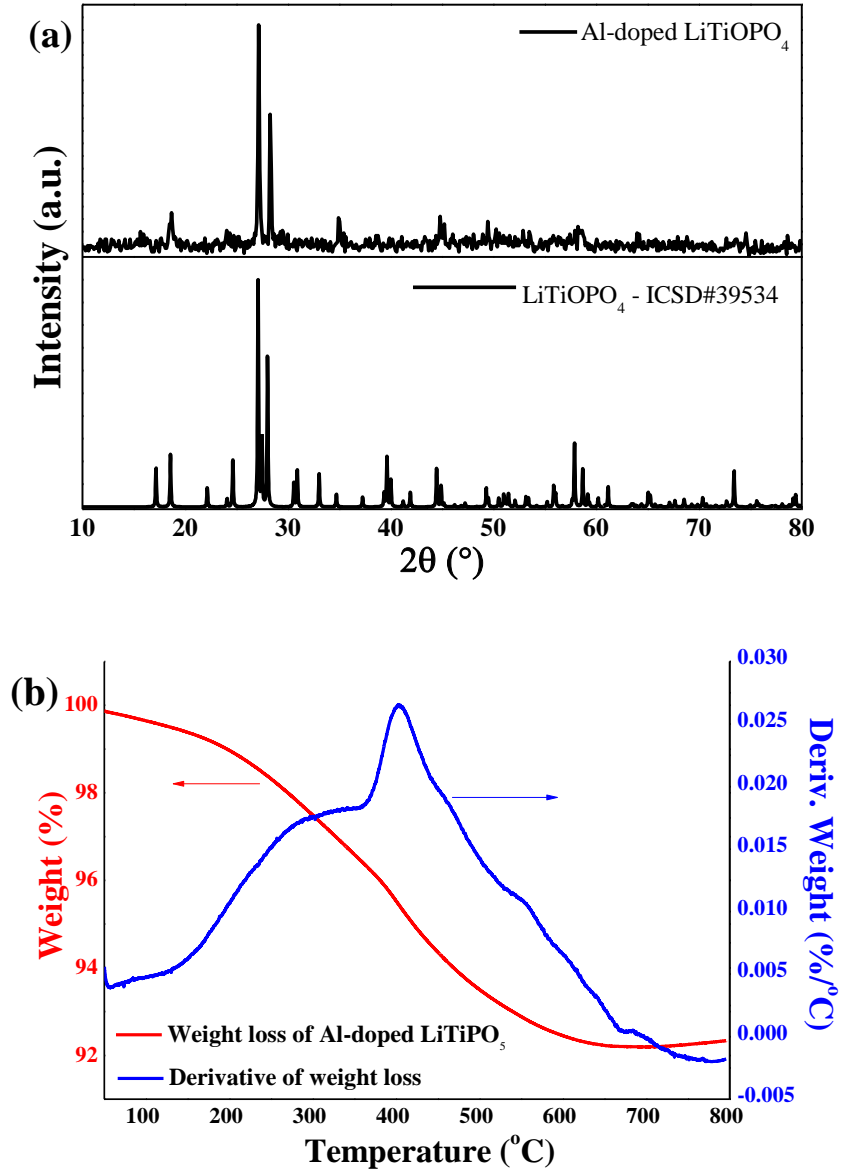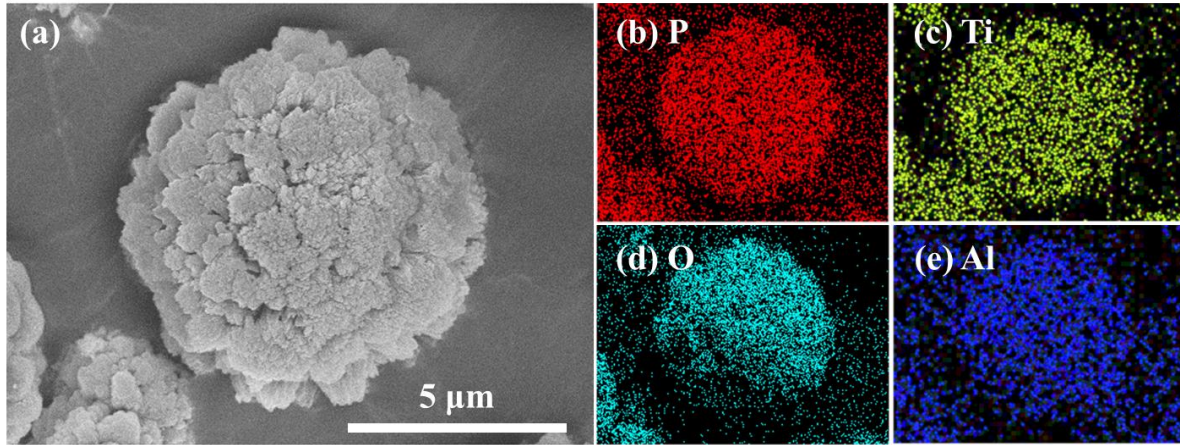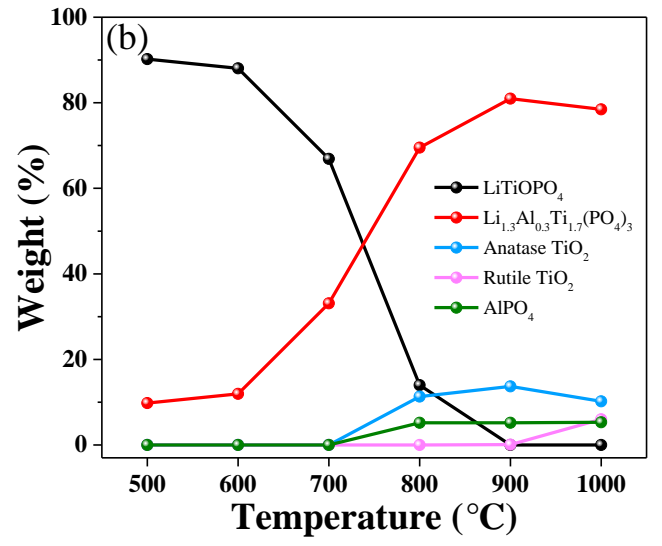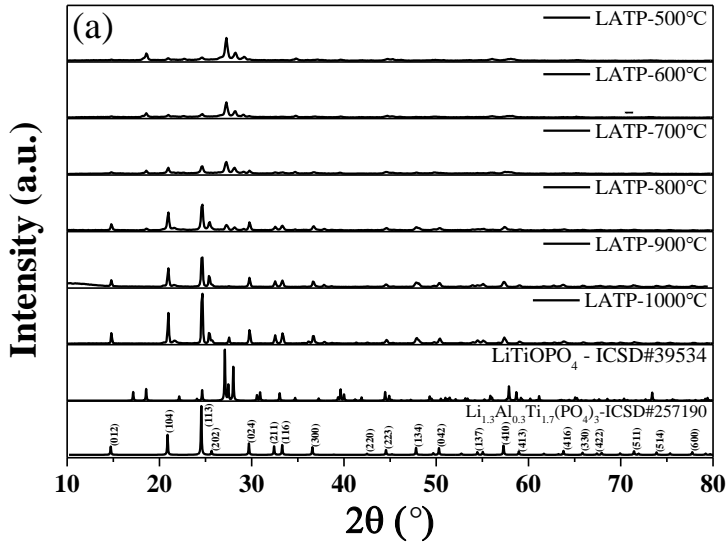
(a)

5 µm

(b) P

(c) Ti
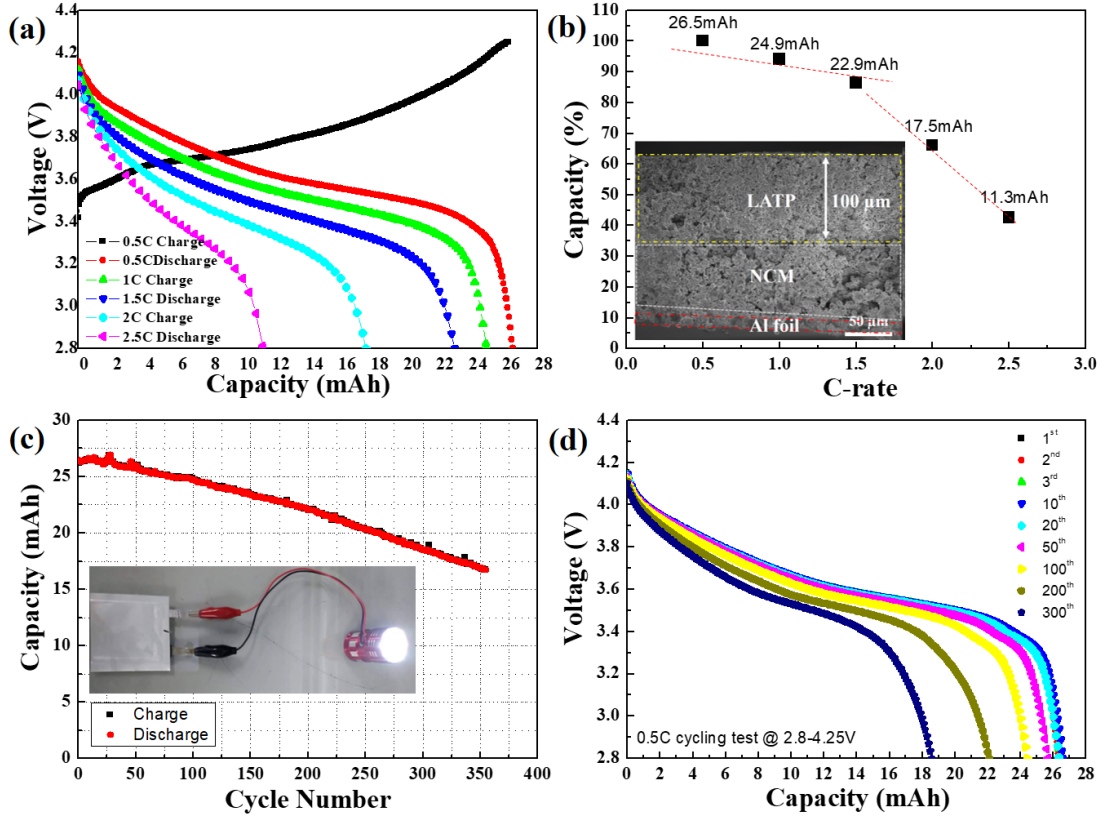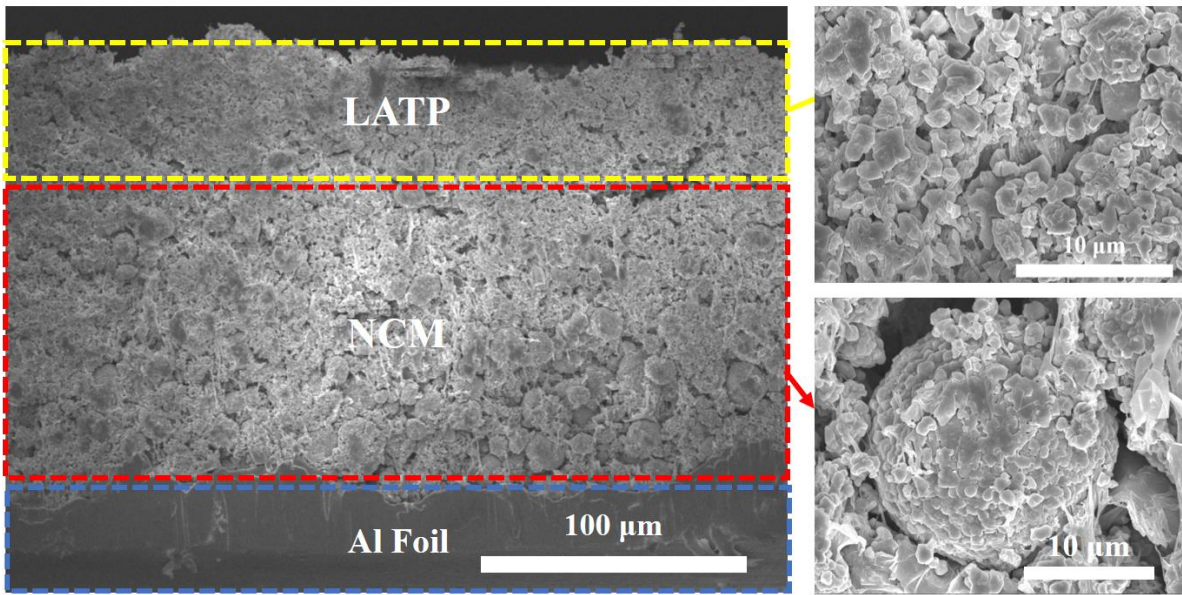
(d) O
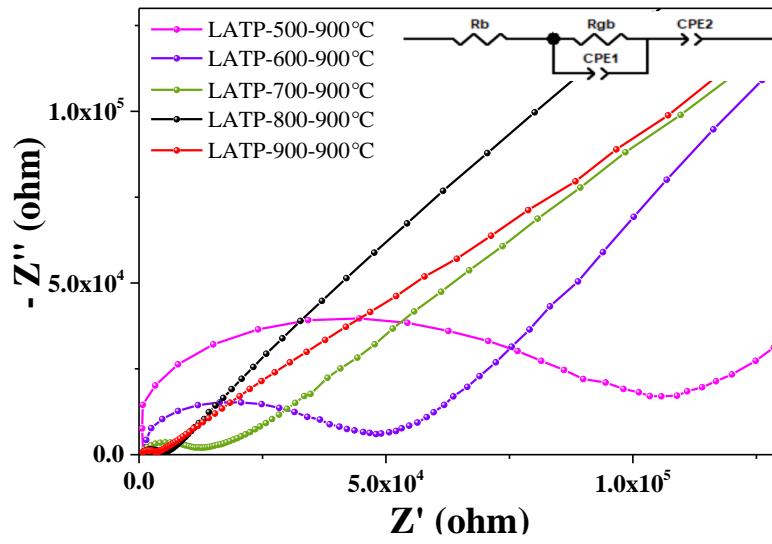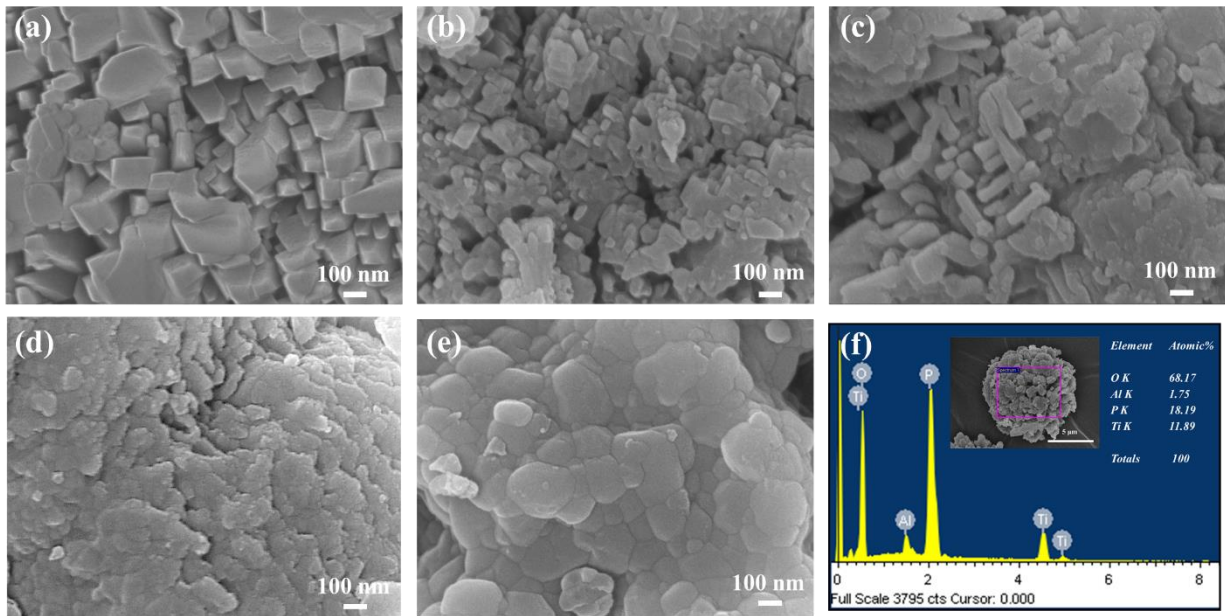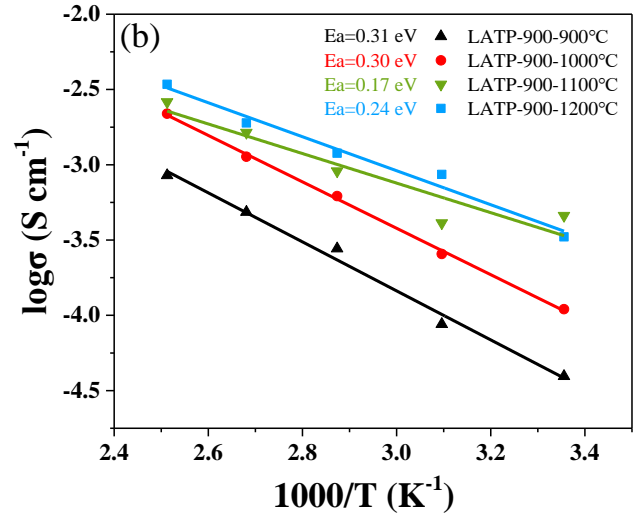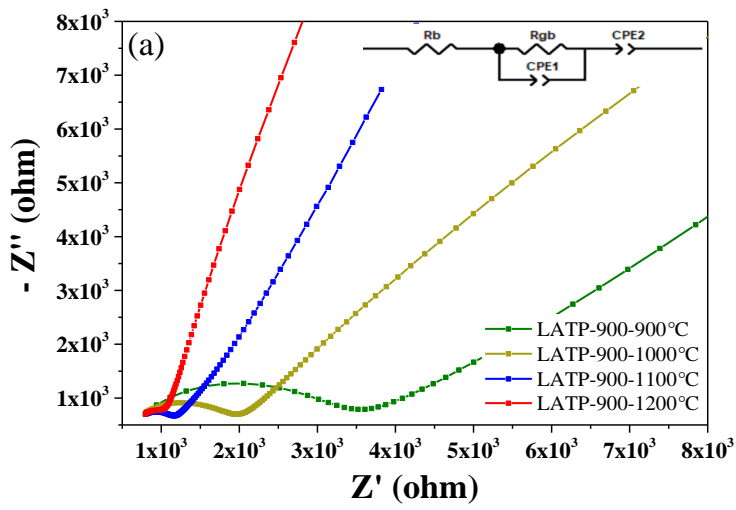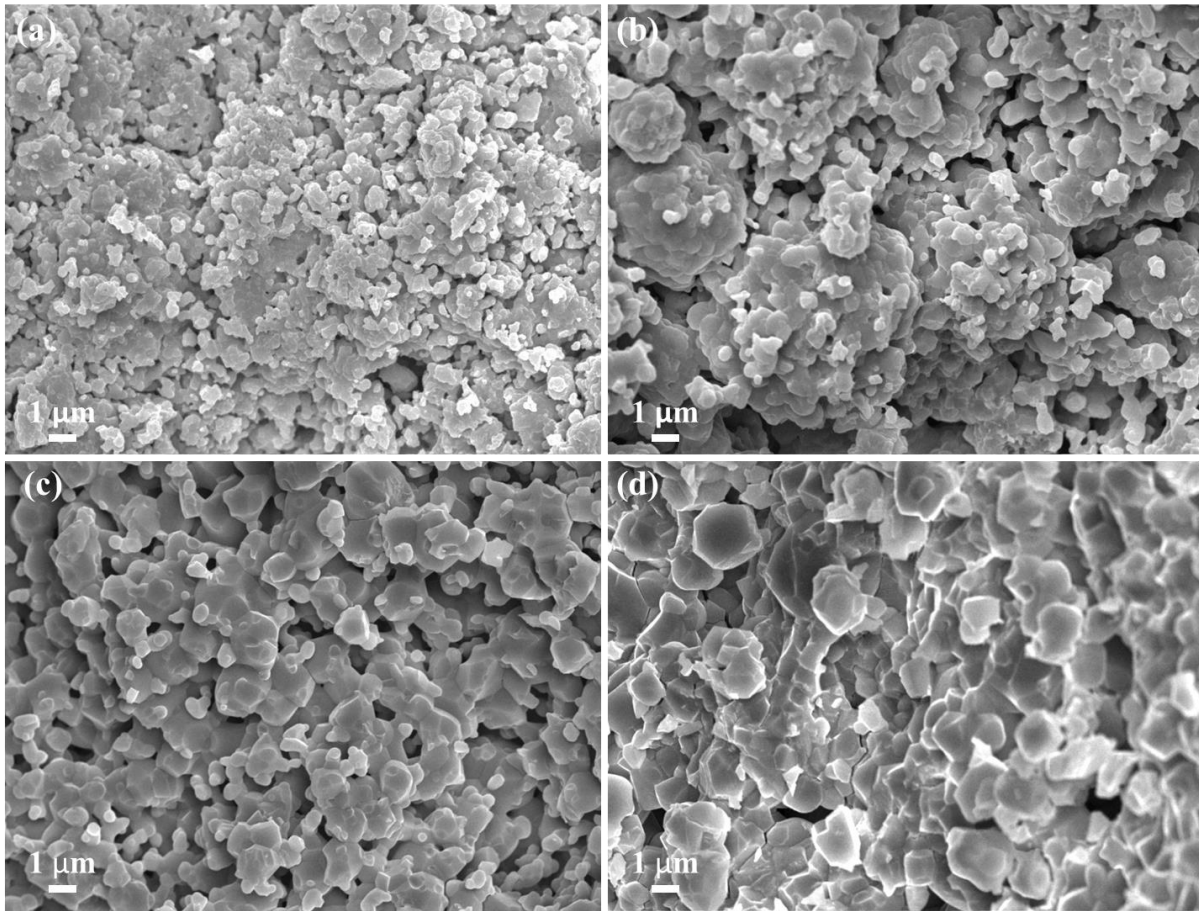
(e) Al

Table. 1 The value of bulk conductivity (σ_{bulk}), grain boundary conductivity (σ_{gb}), total conductivity (σ_{total}) and relative density measured at 25 °C for pellets of LATP-500-900, LATP-600-900, LATP-700-900, LATP-800-900 and LATP-900-900.

	σ_{bulk} (S/cm)	σ_{gb} (S/cm)	σ_{total} (S/cm)	Relative density (%)
LATP-500-900°C	$5.10*10^{-5}$	$1.72*10^{-6}$	$1.67*10^{-6}$	88.04
LATP-600-900°C	$6.95*10^{-5}$	$4.51*10^{-6}$	$4.23*10^{-6}$	88.99
LATP-700-900°C	$1.10*10^{-4}$	$1.79*10^{-5}$	$1.54*10^{-5}$	90.23
LATP-800-900°C	$2.65*10^{-4}$	$4.93*10^{-5}$	$4.15*10^{-5}$	91.01
LATP-900-900°C	$3.24*10^{-4}$	$6.95*10^{-5}$	$5.72*10^{-5}$	94.10

Table. 2. The value of bulk conductivity (σ_{bulk}), grain boundary conductivity (σ_{gb}), total conductivity (σ_{total}) and relative density measured at 25 °C for pellets of LATP-900-900, LATP-900-1000, LATP-900-1100 and LATP-900-1200.

	σ_{bulk} (S/cm)	σ_{gb} (S/cm)	σ_{total} (S/cm)	Relative density (%)
LATP-900-900°C	$3.24*10^{-4}$	$6.95*10^{-5}$	$5.72*10^{-5}$	94.10
LATP-900-1000°C	$5.57*10^{-4}$	$1.56*10^{-4}$	$1.22*10^{-4}$	96.85
LATP-900-1100°C	$6.57*10^{-4}$	$4.59*10^{-4}$	$2.70*10^{-4}$	99.07
LATP-900-1200°C	$9.29*10^{-4}$	$3.32*10^{-4}$	$2.44*10^{-4}$	98.06

Table. 3. Phase composition of LATP powders calcined at 900 °C, pelletised and sintered at different temperatures (1000-1200 °C).

wt.%	LiTiOPO$_4$	Li$_{1.3}$Al$_{0.3}$Ti$_{1.7}$(PO$_4$)$_3$	Anatase TiO$_2$	Rutile TiO$_2$	AlPO$_4$
LATP-900-900°C	0	69.4	10.5	0.8	19.3
LATP-900-1000°C	0	76.6	1.5	12.9	8.9
LATP-900-1100°C	0	70.8	0	15.0	14.2
LATP-900-1200°C	0	57.7	0	10.3	32.0